STABLE INTEGRATED RBF CALCULATION USING PRECONDITIONING AND HIGH-ORDER COMPACT APPROXIMATION FOR SECOND-ORDER PDES

C.M.T. TIEN[1]*, **N. MAI-DUY**[1], **D. NGO-CONG**[1], **C.D. TRAN**[1], **T. TRAN-CONG**[1]

[1]Computational Engineering and Science Research Centre, Faculty of Health, Engineering and Sciences, The University of Southern Queensland, Toowoomba, Queensland 4350, Australia.

* Corresponding author, E-mail address: camminhtri.tien@usq.edu.au

ABSTRACT

It is well known that the accuracy of several radial basis function (RBF) methods, including those based on multiquadric (MQ) RBFs, depends on a free shape parameter. For smooth solutions, it is theoretically claimed that without round-off error the highest accuracy for a given number of nodal points is regularly achieved with extreme values of the shape parameter, where the RBFs become increasingly flat. However, the limit values of the shape parameter (increasingly flat) often leads to very ill-conditioned problems. To alleviate this difficulty, we present a RBF method for solving second-order PDEs, in which (i) the RBF approximations are constructed using the integral approach where the starting points are fourth-order derivatives; and (ii) a simple but effective preconditioning technique is employed in the process of converting the RBF coefficient space into the physical space. In this paper, we first numerically study the effect of the shape parameter on the solution accuracy of the present RBF method through Poisson equation; and, then apply the method employed with extreme values of the shape parameter to simulate several fluid flow problems where highly accurate and stable solutions are produced.

INTRODUCTION

The drawback of element-based computational methods such as finite element method (FEM) or finite volume method (FVM) for the simulation of problems with extremely large deformations or complex geometry is that frequent mesh-updating is required. With these methods, the construction of a mesh in three or more dimensions is also a nontrivial problem. Such difficulties have motivated many researchers to develop so-called element-free methods such as smooth particle hydrodynamic (SPH) (Lucy, 1977), diffusive element method (DEM) (Nayroles *et al.*, 1992), and element-free Galerkin method (EFG) (Belytschko *et al.*, 1994). For an overview on these element-free methods, readers may find more details in (Chen *et al.*, 2006) and references therein. In the context of radial basis function (RBF), (Hardy, 1971) who worked on scattered data fitting and general multi-dimensional data in interpolation problems, devised multiquadric (MQ)-RBF which is a simplest class of element-free methods (Sarler, 2005). Since then, the RBF methods have been developed for solving fluid flow, convective heat transfer (Divo and Kassab, 2007), solid-liquid phase change (Voller *et al.*, 2006), and fluid-structure interpolation (Rendall and Allen, 2008) problems in two- and three-dimensions. Although MQ-RBF methods possess superior convergence rates, their accuracy is dependent on a free parameter (the shape parameter) and its optimal value depends on the function to be interpolated, the nodal points, the RBF, and the machine precision (Buhmann, 1990; Rippa, 1999). An important issue involving the use of RBFs is how to choose an optimal value or even a consistently "good" value of the shape parameter, which has received a great deal of attention of many researchers for the past few decades. In particular, (Rippa, 1999) presented an algorithm for selecting a good value of the shape parameter by minimising a cost function that imitates the error between the radial interpolant and the unknown function. (Driscoll and Fornberg, 2002) theoretically observed the interpolation with extreme values of the shape parameter (increasingly flat) where the differential RBF (here referred to as DRBF) interpolants are usually well-behaved. In (Larsson and Fornberg, 2005), the authors gave an explicit form of the multivariate RBF interpolants in the limit region of the shape parameter, where the RBFs become increasingly flat. Recently, (Fornberg and Wright, 2004) proposed the Contour-Pade algorithm which can stably compute the whole region of the shape parameter on a complex plane. Many different approaches to enhance the stability of DRBF methods have been proposed, for examples (Fasshauer and Mccourt, 2012; Stefano and Gabriele, 2013) and the references therein. For integrated RBF (here referred to as IRBF) approaches, which was first proposed in (Mai-Duy and Tran-Cong, 2001), the studies of (Mai-Duy and Tran-Cong, 2005; Sarra, 2006) numerically showed that the even IRBFs are generally most accurate and most poorly conditioned for large values of the shape parameter, where the RBFs become increasingly flat. However, the authors did not provide a solution to overcome the ill-condition problems when employing the IRBFs in the nearly flat range. It is noted that the integral approach is more accurate than the differential approach, which was studied in (Mai-Duy and Tran-Cong, 2001; Sarra, 2006; Tien *et al.*, 2015a).

This paper presents (i) an easy-to-implement but effective preconditioning technique for the compact IRBF (CIRBF) schemes to alleviate ill-condition problems arising from large values of the shape parameter, where the RBFs become increasingly flat; and, (ii) a combined compact IRBF (CCIRBF) approximation scheme to enhance the solution accuracy in the large value range of the shape parameter (Tien *et al.*, 2015b). Unlike CIRBF schemes previously proposed in (Thai-Quang *et al.*, 2012; Mai-Duy and Tran-Cong, 2013; Tien *et al.*, 2015c), the present preconditioned CCIRBF scheme is able to stably compute second-order PDE problems with much larger values of the shape parameter. We demonstrate the stability and accuracy of the scheme through various numerical experiments.

COMBINED COMPACT INTEGRATED RBF (CCIRBF) SCHEME

The CCIRBF approximation scheme developed by (Tien *et al.*, 2015b) is employed in this work for highly accurate solutions. Readers may find more details about the CCIRBF scheme in the literature, which is summarised here for convenience. Hereafter, for brevity, η denotes either x or y in a generic local stencil $\{\eta_1, \eta_2, \eta_3\}$, where $\eta_1 < \eta_2 < \eta_3$ and $\eta_2 \equiv \eta_{(i,j)}$.

In IRBF approaches, the MQ function is usually chosen as

the basis function

$$G_i(x) = \sqrt{(x - c_i)^2 + a_i^2}, \qquad (1)$$

where c_i and a_i are the centre and the width of the i-th MQ, respectively. On a stencil, the set of nodal points is taken to be the same as the set of MQ centres. The MQ width is defined as $a_i = \beta h_i$, where β, which is the shape parameter, is a positive scalar and h_i is the distance between the i-th node and its closest neighbour.

For second-order PDEs, the integral process of the present CCIRBF starts with the decomposition of fourth-order derivatives of a variable, f, into RBFs

$$\frac{d^4 f(\eta)}{d\eta^4} = \sum_{i=1}^{m} w_i G_i(\eta). \qquad (2)$$

Approximate representations for the second- and first-order derivatives and the functions itself are then obtained through the integration processes

$$\frac{d^2 f(\eta)}{d\eta^2} = \sum_{i=1}^{m} w_i I_{2i}(\eta) + c_1 \eta + c_2, \qquad (3)$$

$$\frac{df(\eta)}{d\eta} = \sum_{i=1}^{m} w_i I_{3i}(\eta) + \frac{1}{2} c_1 \eta^2 + c_2 \eta + c_3, \qquad (4)$$

$$f(\eta) = \sum_{i=1}^{m} w_i I_{4i}(\eta) + \frac{1}{6} c_1 \eta^3 + \frac{1}{2} c_2 \eta^2 + c_3 \eta + c_4, \qquad (5)$$

where $I_{1i}(\eta) = \int G_i(\eta) d\eta$; $I_{2i}(\eta) = \int I_{1i}(\eta) d\eta$; $I_{3i}(\eta) = \int I_{2i}(\eta) d\eta$; $I_{4i}(\eta) = \int I_{3i}(\eta) d\eta$; and c_1, c_2, c_3, and c_4 are the constants of integration.

First-order derivative approximations

For the combined compact approximation of the first-order derivatives at interior nodes, extra information is chosen as not only $\left\{ \frac{df_1}{d\eta}; \frac{df_3}{d\eta} \right\}$ but also $\left\{ \frac{d^2 f_1}{d\eta^2}; \frac{d^2 f_3}{d\eta^2} \right\}$. We construct the conversion system over a 3-point stencil as follows.

$$\begin{bmatrix} f_1 \\ f_2 \\ f_3 \\ \frac{df_1}{d\eta} \\ \frac{df_3}{d\eta} \\ \frac{d^2 f_1}{d\eta^2} \\ \frac{d^2 f_3}{d\eta^2} \end{bmatrix} = \underbrace{\begin{bmatrix} \mathbf{I}_4 \\ \mathbf{I}_3 \\ \mathbf{I}_2 \end{bmatrix}}_{\mathbf{C}} \begin{bmatrix} w_1 \\ w_2 \\ w_3 \\ c_1 \\ c_2 \\ c_3 \\ c_4 \end{bmatrix}, \qquad (6)$$

where $\frac{df_i}{d\eta} = \frac{df}{d\eta}(\eta_i)$ with $i \in \{1, 2, 3\}$; $\mathbf{C}$ is the conversion matrix; and $\mathbf{I}_2$, $\mathbf{I}_3$, and $\mathbf{I}_4$ are integration matrices.

At $\eta = \eta_2$, the approximation formulation of the stencil is expressed in the matrix-vector form as

$$\begin{bmatrix} -\mu_4 & 1 & -\mu_5 \end{bmatrix} \mathbf{f}' + \begin{bmatrix} -\mu_6 & 0 & -\mu_7 \end{bmatrix} \mathbf{f}''$$
$$= \begin{bmatrix} \mu_1 & \mu_2 & \mu_3 \end{bmatrix} \mathbf{f}, \qquad (7)$$

where $\{\mu_i\}_{i=1}^{7}$ is the set of IRBFs in the physical space; $\mathbf{f}' = [f_1', f_2', f_3']^T$; $\mathbf{f}'' = [f_1'', f_2'', f_3'']^T$; and $\mathbf{f} = [f_1, f_2, f_3]^T$.

At the boundary nodes, the first-order derivatives are approximated in special compact stencils. Consider the boundary node, e.g. η_1. Its associated stencil is $\{\eta_1, \eta_2, \eta_3, \eta_4\}$ and extra information is chosen as $\frac{df_2}{d\eta}$ and $\frac{d^2 f_2}{d\eta^2}$. The approxi-

mation formulation of the stencil is expressed in the matrix-vector form as

$$\begin{bmatrix} 1 & -\mu_{sp5} & 0 & 0 \end{bmatrix} \mathbf{f}' + \begin{bmatrix} 0 & -\mu_{sp6} & 0 & 0 \end{bmatrix} \mathbf{f}''$$
$$= \begin{bmatrix} \mu_{sp1} & \mu_{sp2} & \mu_{sp3} & \mu_{sp4} \end{bmatrix} \mathbf{f}, \qquad (8)$$

where $\{\mu_{spi}\}_{i=1}^{6}$ is the set of IRBFs in the physical space; $\mathbf{f}' = [f_1', f_2', f_3', f_4']^T$; $\mathbf{f}'' = [f_1'', f_2'', f_3'', f_4'']^T$; and $\mathbf{f} = [f_1, f_2, f_3, f_4]^T$.

Second-order derivative approximations

For the combined compact approximation of the second-order derivatives at interior nodes, we employ the same extra information used in the approximation of the first-order derivative, involving $\left\{ \frac{df_1}{d\eta}; \frac{df_3}{d\eta} \right\}$ and $\left\{ \frac{d^2 f_1}{d\eta^2}; \frac{d^2 f_3}{d\eta^2} \right\}$. At $\eta = \eta_2$, the approximation formulation of the stencil is expressed in the matrix-vector form as

$$\begin{bmatrix} -\nu_4 & 0 & -\nu_5 \end{bmatrix} \mathbf{f}' + \begin{bmatrix} -\nu_6 & 1 & -\nu_7 \end{bmatrix} \mathbf{f}''$$
$$= \begin{bmatrix} \nu_1 & \nu_2 & \nu_3 \end{bmatrix} \mathbf{f}, \qquad (9)$$

where $\{\nu_i\}_{i=1}^{7}$ is the set of IRBFs in the physical space; $\mathbf{f}' = [f_1', f_2', f_3']^T$; $\mathbf{f}'' = [f_1'', f_2'', f_3'']^T$; and $\mathbf{f} = [f_1, f_2, f_3]^T$.

At the boundary nodes, i.e. $\eta = \eta_1$, we employ the same special stencil, i.e. $\{\eta_1, \eta_2, \eta_3, \eta_4\}$, and extra information, i.e. $\frac{df_2}{d\eta}$ and $\frac{d^2 f_2}{d\eta^2}$, used in the approximation of the first-order derivatives. The approximation formulation of the stencil is expressed in the matrix-vector form as

$$\begin{bmatrix} 0 & -\nu_{sp5} & 0 & 0 \end{bmatrix} \mathbf{f}' + \begin{bmatrix} 1 & -\nu_{sp6} & 0 & 0 \end{bmatrix} \mathbf{f}''$$
$$= \begin{bmatrix} \nu_{sp1} & \nu_{sp2} & \nu_{sp3} & \nu_{sp4} \end{bmatrix} \mathbf{f}, \qquad (10)$$

where $\{\nu_{spi}\}_{i=1}^{6}$ is the set of IRBFs in the physical space; $\mathbf{f}' = [f_1', f_2', f_3', f_4']^T$; $\mathbf{f}'' = [f_1'', f_2'', f_3'', f_4'']^T$; and $\mathbf{f} = [f_1, f_2, f_3, f_4]^T$.

Matrix assembly for first- and second-order derivative approximations

The IRBF system on a grid line for the first- and second-order derivatives is obtained as follows.

$$\underbrace{\begin{bmatrix} \mathbf{A}_1 & \mathbf{B}_1 \\ \mathbf{A}_2 & \mathbf{B}_2 \end{bmatrix}}_{\text{Coefficient matrix}} \begin{bmatrix} \mathbf{f}' \\ \mathbf{f}'' \end{bmatrix} = \begin{bmatrix} \mathbf{R}_1 \\ \mathbf{R}_2 \end{bmatrix} \mathbf{f}, \qquad (11)$$

where $\mathbf{A}_1$, $\mathbf{A}_2$, $\mathbf{B}_1$, $\mathbf{B}_2$, $\mathbf{R}_1$, and $\mathbf{R}_2$ are $n_\eta \times n_\eta$ matrices; $\mathbf{f}' = \left[f_1', f_2', ..., f_{n_\eta}' \right]^T$; $\mathbf{f}'' = \left[f_1'', f_2'', ..., f_{n_\eta}'' \right]^T$; and $\mathbf{f} = \left[f_1, f_2, ..., f_{n_\eta} \right]^T$. The coefficient matrix is sparse with diagonal sub-matrices. Solving (11) yields

$$\mathbf{f}' = \mathbf{D}_\eta \mathbf{f}, \qquad (12)$$

$$\mathbf{f}'' = \mathbf{D}_{\eta\eta} \mathbf{f}, \qquad (13)$$

where $\mathbf{D}_\eta$ and $\mathbf{D}_{\eta\eta}$ are $n_\eta \times n_\eta$ matrices. The approximations of the first- and second-order derivatives, (12) and (13), will be used in the following sections.

PRECONDITIONING TECHNIQUE FOR CCIRBF

A new equivalent conversion system is constructed by multiplying a preconditioning matrix $\mathbf{C}^{*-1}$ to both sides of the

original conversion system (6) as follows.

$$\mathbf{C}^{*-1} \begin{bmatrix} f_1 \\ f_2 \\ f_3 \\ \frac{df_1}{d\eta} \\ \frac{df_3}{d\eta} \\ \frac{d^2 f_1}{d\eta^2} \\ \frac{d^2 f_3}{d\eta^2} \end{bmatrix} = \underbrace{\mathbf{C}^{*-1}\mathbf{C}}_{\mathbf{C}_p} \begin{bmatrix} w_1 \\ w_2 \\ w_3 \\ c_1 \\ c_2 \\ c_3 \\ c_4 \end{bmatrix}, \qquad (14)$$

where $\mathbf{C}$ is the original conversion matrix in (6); $\mathbf{C}^{*-1}$ is the preconditioning matrix which has exactly the same form with the original conversion matrix $\mathbf{C}$ but uses a different value of β. Usually, β used in $\mathbf{C}^{*-1}$ is chosen to be small, for example $\beta = 10$ so that its corresponding condition number is in a well-behaved range; and, $\mathbf{C}_p$ is a new conversion matrix. By this way, the new conversion matrix $\mathbf{C}_p$ is able to bypass the ill-condition problems when β in the original conversion matrix $\mathbf{C}$ becomes large.

It is noted that the proposed preconditioning technique is only needed when one implements the CCIRBF in the large value range of β where the ill-condition problems occur. In the small value range of β,

NUMERICAL EXAMPLES

We evaluate the performance of the present scheme through the following measures

i. the root mean square error (*RMS*) is defined as

$$RMS = \sqrt{\frac{\sum_{i=1}^{N} \left(f_i - \overline{f}_i\right)^2}{N}}, \qquad (15)$$

where f_i and $\overline{f}_i$ are the computed and exact values of the solution f at the i-th node, respectively; and, N is the number of nodes over the whole domain.

ii. the global convergence rate with respect to the grid refinement is defined through

$$Error(h) \approx \gamma h^\alpha = O(h^\alpha). \qquad (16)$$

where h is the grid size; and γ and α are exponential model's parameters.

For comparison purposes, we also implement the DRBF scheme of (Kansa, 1990) and CIRBF scheme of (Thai-Quang *et al.*, 2012) for numerical calculations. It is noted that the proposed preconditioning technique described in the previous Section is applied for the CIRBF-Precond version. In Taylor-Green vortex flows, we choose a large shape parameter, $\beta = 500$, for the original conversion matrix $\mathbf{C}$ and a small shape parameter, $\beta = 10$, for the preconditioning matrix $\mathbf{C}^{*-1}$. In irregular bottom lid driven cavity flows, we choose a large shape parameter, $\beta = 1000$, for the original conversion matrix $\mathbf{C}$ and a small shape parameter, $\beta = 10$, for the preconditioning matrix $\mathbf{C}^{*-1}$. In these two fluid flow problems, we employ the fully coupled procedure which was detailed in (Tien *et al.*, 2015a) to calculate Navier-Stokes (NS) equations. For convenience, the fully coupled approach for NS equations is summarised in the matrix-vector form as follows.

$$\begin{bmatrix} \mathbf{K} & \mathbf{0} & \mathbf{G}_x \\ \mathbf{0} & \mathbf{K} & \mathbf{G}_y \\ \mathbf{D}_x & \mathbf{D}_y & \mathbf{0} \end{bmatrix} \begin{bmatrix} \mathbf{u}^n \\ \mathbf{v}^n \\ \mathbf{p}^{n-\frac{1}{2}} \end{bmatrix} = \begin{bmatrix} \mathbf{r}_x^n \\ \mathbf{r}_y^n \\ \mathbf{0} \end{bmatrix}, \qquad (17)$$

where

$$\mathbf{K} = \frac{1}{\Delta t}\left\{\mathbf{I} - \frac{\Delta t}{2Re}\mathbf{L}\right\}, \qquad (18)$$

$$\mathbf{r}_x^n = \frac{1}{\Delta t}\left\{\mathbf{I} + \frac{\Delta t}{2Re}\mathbf{L}\right\}\mathbf{u}^{n-1} - \left\{\frac{3}{2}\mathbf{N}(\mathbf{u}^{n-1}) - \frac{1}{2}\mathbf{N}(\mathbf{u}^{n-2})\right\}, \qquad (19)$$

$$\mathbf{r}_y^n = \frac{1}{\Delta t}\left\{\mathbf{I} + \frac{\Delta t}{2Re}\mathbf{L}\right\}\mathbf{v}^{n-1} - \left\{\frac{3}{2}\mathbf{N}(\mathbf{v}^{n-1}) - \frac{1}{2}\mathbf{N}(\mathbf{v}^{n-2})\right\}, \qquad (20)$$

n denotes the current time level; $\mathbf{u}^n$, $\mathbf{v}^n$ are velocity vectors in the x- and y-directions; $p^{n-\frac{1}{2}}$ is pressure vector; $\mathbf{I}$ is the identity matrix; and $\mathbf{N}$ and $\mathbf{L}$ are the matrix operators for the approximation of the convective and diffusive terms, respectively.

In this work, calculations are done with a Dell computer, Precision T7500. Its specifications are Intel(R) Xeon(R) CPU E5507/ 2.26 GHz, memory(RAM) of 128GB and 64-bit operating system. The Matlab(R) version 2014 is utilised.

Poisson equation in two dimensions

In order to study the 2D spatial accuracy of the present CCIRBF approximation schemes over a wide value range of the shape parameter, we consider the following Poisson equation

$$\frac{d^2 f}{dx_1^2} + \frac{d^2 f}{dx_2^2} = -2\pi^2 \cos(\pi x_1)\cos(\pi x_2), \qquad (21)$$

on a square domain $[0,1]^2$, subjected to the Dirichlet boundary condition derived from the following exact solution

$$\overline{f} = \cos(\pi x_1)\cos(\pi x_2). \qquad (22)$$

The calculations are carried out on a uniform grid of 101×101. A set of β of $[1, 101, 201, ..., 2001]$ is chosen. The top of Figure 1 shows the effect of β on the condition number of the conversion matrix, where we can see that the present CCIRBF-Precond has much lower condition number than the "pure" CCIRBF. The bottom of Figure 1 illustrates that the present CCIRBF-Precond scheme is much more accurate than the DRBF, CIRBF and CIRBF-Precond schemes. In addition, these Figures also indicate that the preconditioning technique has the ability to improve the accuracy and stability of the CCIRBF and CIRBF in the large value range of β.

Taylor-Green vortex

To study the performance of the present CCIRBF approximation in simulating viscous flows in a rectangular domain, we consider a transient viscous flow problem, namely Taylor-Green vortex (TGV) which is governed by NS equations and has the analytical solutions as follows.

$$\overline{u}(x_1, x_2, t) = -\cos(kx_1)\sin(kx_2)\exp(-2k^2 t/Re), \qquad (23)$$

$$\overline{v}(x_1, x_2, t) = \sin(kx_1)\cos(kx_2)\exp(-2k^2 t/Re), \qquad (24)$$

$$\overline{p}(x_1, x_2, t) = -1/4\left\{\cos(2kx_1) + \cos(2kx_2)\right\}\exp(-4k^2 t/Re), \qquad (25)$$

where $0 \leq x_1, x_2 \leq 2\pi$. Calculations are carried out for $k = 2$ on a set of uniform grids, $\{11 \times 11, 21 \times 21, ..., 51 \times 51\}$. A fixed time step $\Delta t = 0.002$ and $Re = 100$ are employed. Numerical solutions are computed at $t = 2$. The exact solution, i.e. equations (23)-(25), provides the initial fields at $t = 0$ and the time-dependent boundary conditions. Table 1 shows
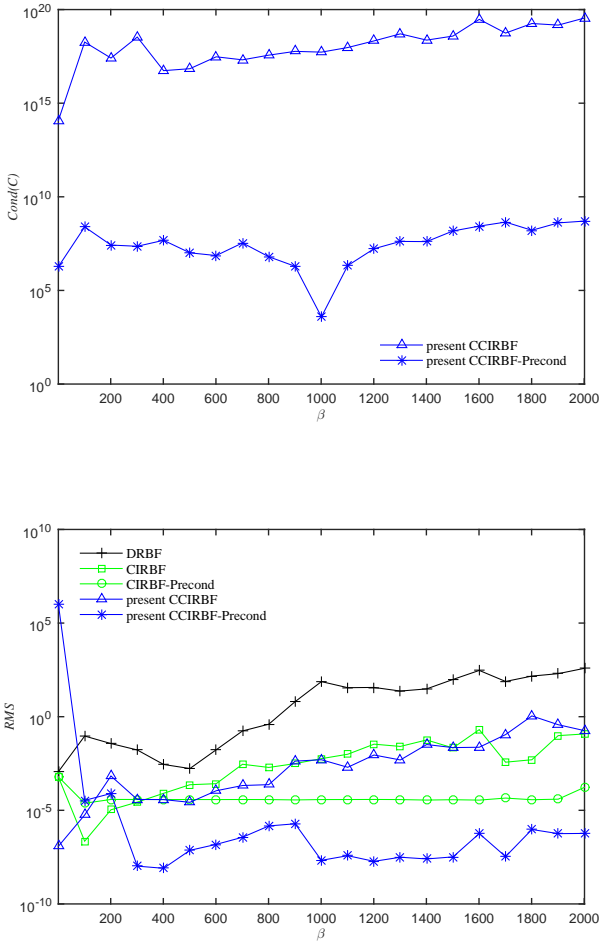
Figure 1: 2D Poisson equation, 101×101: The effect of β on the condition number of the conversion matrix (top) and on the solution accuracy *RMS* (bottom).

Table 1: Taylor-Green vortex: *RMS* errors and convergence rates.

HOC (Tian et al., 2011)			
Grid	*u*-error	*v*-error	*p*-error
11×11	7.0070489E-02	7.0070489E-02	1.0764149E-01
21×21	9.0692193E-03	9.0692193E-03	1.0567607E-02
31×31	2.8851487E-03	2.8851487E-03	2.9103288E-03
41×41	1.2238736E-03	1.2238736E-03	1.1356134E-03
51×51	6.3063026E-04	6.3063026E-04	5.3933641E-04
Rate	$O(h^{2.92})$	$O(h^{2.92})$	$O(h^{3.28})$
present CCIRBF using $\beta = 500$			
Grid	*u*-error	*v*-error	*p*-error
11×11	9.0757315E-02	9.0757322E-02	2.3542625E-01
21×21	3.8338024E-03	3.8338114E-03	1.3288235E-02
31×31	1.0201809E-03	1.0201870E-03	3.3851835E-03
41×41	3.6194151E-04	3.6194102E-04	1.4603595E-03
51×51	1.5492043E-04	1.5482812E-04	4.1378984E-04
Rate	$O(h^{3.91})$	$O(h^{3.91})$	$O(h^{3.81})$

obtained by the present method are compared with those reported in (Shyy *et al.*, 1996; Mariani and Prata, 2008; Tien *et al.*, 2015a), where appropriate. From the literature, the FVM results using the well-tested body-fitted coordinate formulation and dense grid of 121×121 presented in (Shyy *et al.*, 1996) have been considered as "Benchmark" results for comparison purposes. Table 2 shows the present results
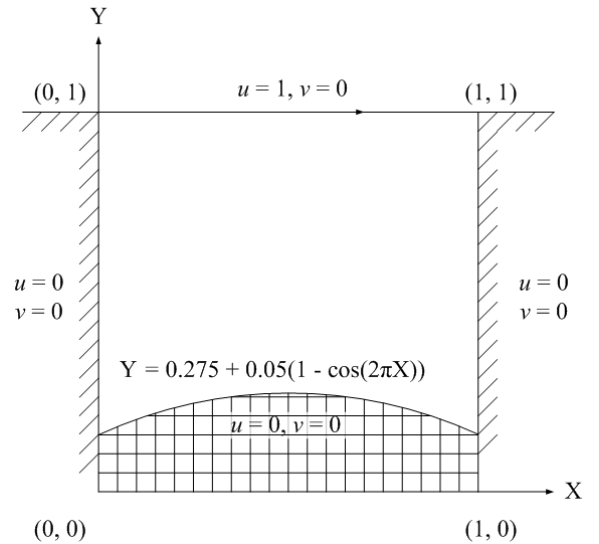

Figure 2: Irregular bottom lid driven cavity: problem configuration and boundary conditions.

for the extrema of the vertical and horizontal velocity profiles along the vertical centreline of the cavity. With relatively low numbers of grids, the results obtained by the present scheme are very comparable with other schemes using much higher numbers of grids.

Figure 4 displays horizontal and vertical velocity profiles along the vertical centreline for different grid sizes, where a grid convergence of the present scheme is obviously observed. The present scheme effectively achieves the benchmark results with a grid of only 83×83 in comparison with the grid of 121×121 used to obtain the benchmark results in (Shyy *et al.*, 1996). In addition, the present results with a grid of only 53×53 outperform those of (Mariani and Prata, 2008) using the grid of 100×100. To exhibit contour plots of the flow, we employ the grid of 83×83. Figures 5 and 6 show streamlines (which are derived from the velocity) and pressure deviation contours, respectively. These plots are in close agreement with those reported in the literature. Figure
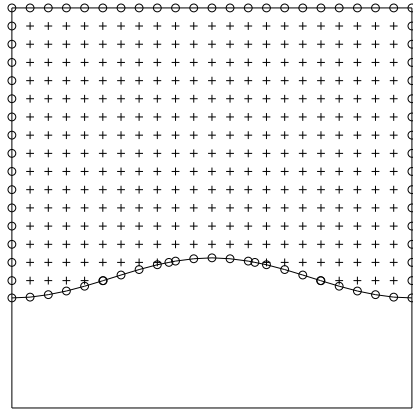
the accuracy comparison between the present scheme and the high-order compact finite difference scheme (HOC) of (Tian *et al.*, 2011). It is seen that the present scheme produces much better accuracy than the HOC; and, its convergence rates are also much higher than those of the HOC, i.e. $O(h^{3.91})$ compared to $O(h^{2.92})$ for the *u*- and *v*-velocities and $O(h^{3.81})$ compared to $O(h^{3.28})$ for the pressure.

Irregular bottom lid driven cavity

The lid driven cavity with a deformed base presented in (Shyy *et al.*, 1996) is chosen to validate the performance of the present approximation scheme in simulating fluid flow problem in an irregular domain. The base is deformed sinusoidally with an amplitude of 10 percent of the base. The computational domain and boundary conditions are illustrated in Figure 2. The boundary nodes are generated through the intersection of the grid lines and the boundary as demonstrated in Figure 3. The interior nodes falling within a small distance $\delta = h/8$, where h is the grid size, to the boundary will also be discarded. A range of uniform grids, $\{53 \times 53, 63 \times 63, 83 \times 83, 93 \times 93\}$ is employed in the simulation. A fixed time step and Reynolds number are chosen to be $\Delta t = 0.001$ and $Re = 1000$, respectively. The results

4

Figure 3: Irregular bottom lid driven cavity, spatial discretisation: + represents for interior nodes; ○ represents for boundary nodes.

Table 2: Irregular bottom lid driven cavity, $\beta = 1000$, $Re = 1000$: Extrema of the vertical and horizontal velocity profiles along the vertical centreline of the cavity. For the CCIRBF, indicative CPU time for corresponding grid is reported in brackets. Minute is abbreviated as m. It is noted that FVM results of (Mariani and Prata, 2008; Shyy *et al.*, 1996) are extracted from Figures in the literature.

Method	Grid	u_{min}	y_{min}
Present CCIRBF (CPU time 47 m)	53×53	-0.3781442	0.4975
Present CCIRBF (CPU time 94 m)	63×63	-0.3924106	0.4959
Present CCIRBF (CPU time 421 m)	83×83	-0.3958749	0.4951
Present CCIRBF (CPU time 482 m)	93×93	-0.3979039	0.4949
CIRBF (Tien *et al.*, 2015a)	53×53	-0.3695975	0.4989
CIRBF (Tien *et al.*, 2015a)	63×63	-0.3847773	0.4967
CIRBF (Tien *et al.*, 2015a)	83×83	-0.3950552	0.4953
CIRBF (Tien *et al.*, 2015a)	93×93	-0.3972010	0.4950
FVM (Mariani and Prata, 2008)	100×100	≈ -0.3524	≈ 0.4929
Benchmark FVM (Shyy *et al.*, 1996)	121×121	≈ -0.3808	≈ 0.5017
Method	Grid	v_{max}	y_{max}
Present CCIRBF (CPU time 47 m)	53×53	0.2180640	0.5601
Present CCIRBF (CPU time 94 m)	63×63	0.2214069	0.5563
Present CCIRBF (CPU time 421 m)	83×83	0.2274348	0.5547
Present CCIRBF (CPU time 482 m)	93×93	0.2292693	0.5549
CIRBF (Tien *et al.*, 2015a)	53×53	0.2165344	0.5638
CIRBF (Tien *et al.*, 2015a)	63×63	0.2239138	0.5589
CIRBF (Tien *et al.*, 2015a)	83×83	0.2282167	0.5555
CIRBF (Tien *et al.*, 2015a)	93×93	0.2286893	0.5548
FVM (Mariani and Prata, 2008)	100×100	—	—
Benchmark FVM (Shyy *et al.*, 1996)	121×121	≈ 0.2362	≈ 0.5610

Figure 4: Irregular bottom lid driven cavity, $\beta = 1000$, $Re = 1000$: Profiles of the u-velocity (top) and v-velocity (bottom) along the vertical centreline as the grid density increases. It is noted that the curves for the last two grids are indistinguishable and in good agreement with the benchmark results of (Shyy *et al.*, 1996).

7 shows the iso-vorticity lines of the present simulation.

CONCLUSION

In this work, we successfully implement the CCIRBF-Precond scheme that works with large values of the shape parameter, $\beta = 500$ and $\beta = 1000$, for the simulation of several fluid flow problems. In these examples, the present method performs significantly better than the HOC and CIRBF schemes. This present robust and highly accurate element-free procedure based on MQ RBFs is promising for many science and engineering problems governed by PDEs.

REFERENCES

BELYTSCHKO, T. *et al.* (1994). "Element-free galerkin methods". *Int. J. Numer. Meth. Eng.*, **37**, 229–256.

BUHMANN, M. (1990). "Multivariate interpolation in odd-dimensional euclidean spaces using multiquadrics". *Constr. Approx.*, **6(1)**, 21–34.

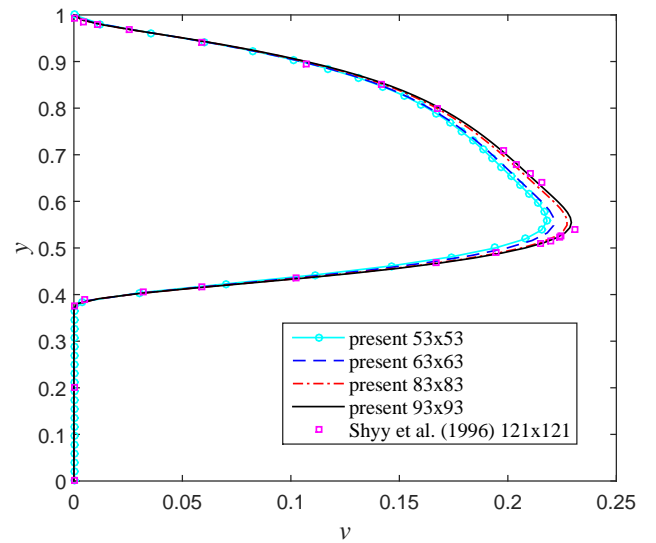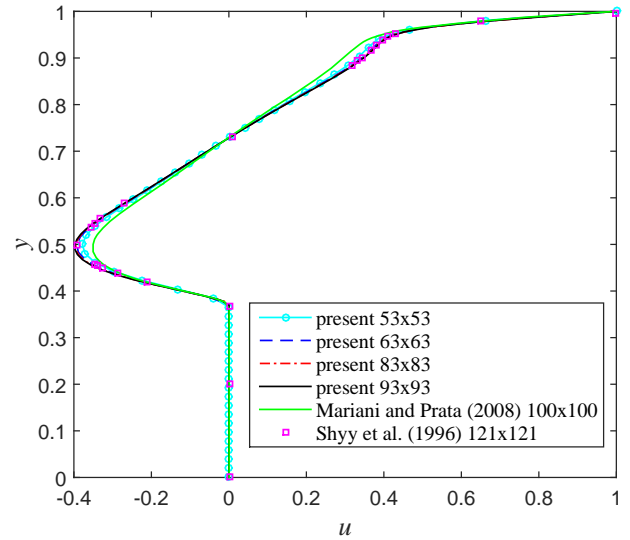CHEN, Y. *et al.* (2006). *Meshless methods in solid mechanics*. Springer, NY 10013, USA.

DIVO, E. and KASSAB, A.J. (2007). "An efficient localized radial basis function meshless method for fluid flow and conjugate heat transfer". *J. Heat Trans.*, **129(2)**, 124–136.

DRISCOLL, T. and FORNBERG, B. (2002). "Interpolation in the limit of increasingly flat radial basis functions". *Comput. Math. Appl.*, **43(3–5)**, 413–422.

FASSHAUER, G. and MCCOURT, M. (2012). "Stable evaluation of gaussian radial basis function interpolants". *SIAM J. Sci. Comput.*, **34(2)**, 737–762.

FORNBERG, B. and WRIGHT, G. (2004). "Stable computation of multiquadric interpolants for all values of the shape parameter". *Comput. Math. Appl.*, **48(5–6)**, 853–867.

HARDY, R. (1971). "Multiquadric equations of topography and other irregular surfaces". *J. Geophys. Res.*, **76(8)**, 1905–1915.

KANSA, E. (1990). "Multiquadrics-a scattered data approximation scheme with applications to computational fluid-dynamics-i. surface approximations and partial derivative estimates". *Comput. Math. Appl.*, **19(8–9)**, 127–145.

LARSSON, E. and FORNBERG, B. (2005). "Theoretical and computational aspects of multivariate interpolation
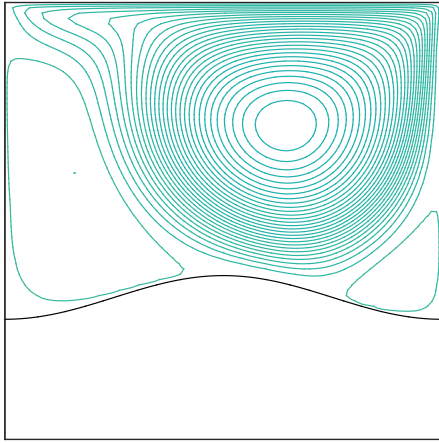
Figure 5: Irregular bottom lid driven cavity, $\beta = 1000$, $Re = 1000$: Streamlines of the flow with the grid of 83×83. The plot contains 30 contour lines whose levels vary linearly from the minimum to maximum values; and, it is in good agreement with that of (Shyy *et al.*, 1996).
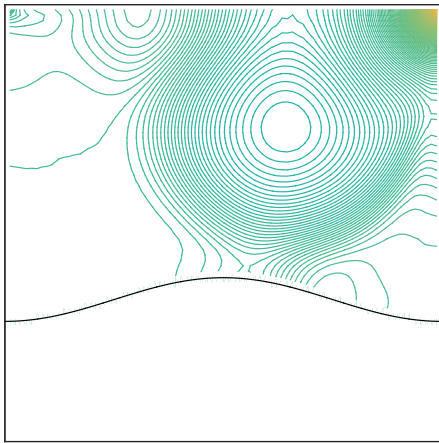

Figure 6: Irregular bottom lid driven cavity, $\beta = 1000$, $Re = 1000$: Static pressure contours of the flow with the grid of 83×83. The plot contains 160 contour lines whose levels vary linearly from the minimum to maximum values.
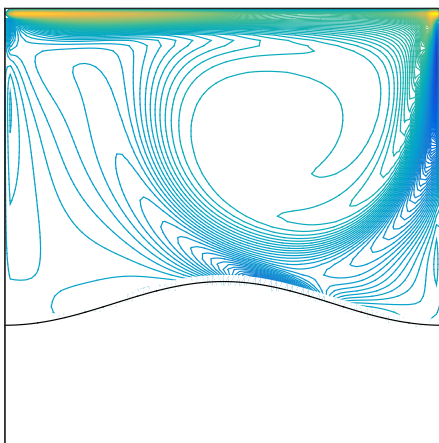

Figure 7: Irregular bottom lid driven cavity, $\beta = 1000$, $Re = 1000$: Iso-vorticity lines of the flow with the grid of 83×83. The plot contains 160 contour lines whose levels vary linearly from the minimum to maximum values.

with increasingly flat radial basis functions". *Comput. Math. Appl.*, **49**, 103–130.

LUCY, L.B. (1977). "A numerical approach to the testing of the fission hypothesis". *Astron. J.*, **82(12)**, 1013–1024.

MAI-DUY, N. and TRAN-CONG, T. (2001). "Numerical solution of differential equations using multiquadric radial basis function networks". *Neural Networks*, **14**, 185–199.

MAI-DUY, N. and TRAN-CONG, T. (2005). "An efficient indirect rbfn-based method for numerical solution of pdes". *Numer. Meth. Part. D. E.*, **21**, 770–790.

MAI-DUY, N. and TRAN-CONG, T. (2013). "A compact five-point stencil based on integrated rbfs for 2d second-order differential problems". *J. Comput. Phys.*, **235**, 302–321.

MARIANI, V. and PRATA, A. (2008). "A Eulerian-Lagrangian method applied to fluid flow in lid-driven cavities with irregular bottom walls". *Numer. Heat Tr. B- Fund.*, **53**, 206–233.

NAYROLES, B. *et al.* (1992). "Generalizing the finite element method: Diffuse approximation and diffuse elements". *Comput. Mech.*, **10(5)**, 307–318.

RENDALL, T. and ALLEN, C. (2008). "Unified fluid–structure interpolation and mesh motion using radial basis functions". *Int. J. Numer. Meth. Eng.*, **74(10)**, 1519–1559.

RIPPA, S. (1999). "An algorithm for selecting a good value for the parameter c in radial basis function interpolation". *Adv. Comput. Math.*, **11**, 193–210.

SARLER, B. (2005). "A radial basis function collocation approach in computational fluid dynamics". *Comput. Model. Eng. Sci.*, **7**, 185–93.

SARRA, S. (2006). "Integrated multiquadric radial basis function approximation methods". *Comput. Math. Appl.*, **51**, 1283–1296.

SHYY, W. *et al.* (1996). *Computational fluid dynamics with moving boundaries.* Taylor&Francis, 1900 Frost Road, Suite 101, Bristol, PA 19007-1598.

STEFANO, D. and GABRIELE, S. (2013). "A new stable basis for radial basis function interpolation". *J. Comput. Appl. Math.*, **253**, 1–13.

THAI-QUANG, N. *et al.* (2012). "High-order alternating direction implicit method based on compact integrated-rbf approximations for unsteady/steady convection-diffusion equations". *Comput. Model. Eng. Sci.*, **89(3)**, 189–220.

TIAN, Z. *et al.* (2011). "A higher order compact finite difference algorithm for solving the incompressible navier stokes equations". *Int. J. Numer. Meth. Eng.*, **88**, 511–532.

TIEN, C.M.T. *et al.* (2015a). "High-order fully coupled scheme based on compact integrated rbf approximation for viscous flows in regular and irregular domains". *Comput. Model. Eng. Sci.*, **105(4)**, 301–340.

TIEN, C.M.T. *et al.* (2015b). "A numerical study of compact approximations based on flat integrated radial basis functions for second-order differential equations". *(submitted to Comput. Math. Appl.).*

TIEN, C.M.T. *et al.* (2015c). "A three-point coupled compact integrated rbf scheme for second-order differential problems". *Comput. Model. Eng. Sci.*, **104(6)**, 425–469.

VOLLER, V. *et al.* (2006). "Meshless local radial basis function collocation method for convective-diffusive solid-liquid phase change problems". *Int. J. Numer. Meth. H.*, **16(5)**, 617–640.